A&A 592, A89 (2016)
DOI: 10.1051/0004-6361/201628703

Astronomy & Astrophysics

iPTF15dtg: a double-peaked Type Ic supernova from a massive progenitor

F. Taddia[1], C. Fremling[1], J. Sollerman[1], A. Corsi[2], A. Gal-Yam[3], E. Karamehmetoglu[1], R. Lunnan[4], B. Bue[5], M. Ergon[1], M. Kasliwal[6], P. M. Vreeswijk[3], and P. R. Wozniak[7]

[1] The Oskar Klein Centre, Department of Astronomy, Stockholm University, AlbaNova, 10691 Stockholm, Sweden
e-mail: francesco.taddia@astro.su.se
[2] Department of Physics, Texas Tech University, Box 41051, Lubbock, TX 79409-1051, USA
[3] Department of Particle Physics & Astrophysics, Weizmann Institute of Science, 76100 Rehovot, Israel
[4] Astronomy Department, California Institute of Technology, Pasadena, CA 91125, USA
[5] Jet Propulsion Laboratory, California Institute of Technology, Pasadena, CA 91109, USA
[6] Cahill Center for Astrophysics, California Institute of Technology, Pasadena, CA 91125, USA
[7] Los Alamos National Laboratory, MS D436, Los Alamos, NM 87545, USA

Received 13 April 2016 / Accepted 31 May 2016

ABSTRACT

Context. Type Ic supernovae (SNe Ic) arise from the core-collapse of H- (and He-) poor stars, which could either be single Wolf-Rayet (WR) stars or lower-mass stars stripped of their envelope by a companion. Their light curves are radioactively powered and usually show a fast rise to peak (∼10−15 d), without any early (in the first few days) emission bumps (with the exception of broad-lined SNe Ic) as sometimes seen for other types of stripped-envelope SNe (e.g., Type IIb SN 1993J and Type Ib SN 2008D).
Aims. We have studied iPTF15dtg, a spectroscopically normal SN Ic with an early excess in the optical light curves followed by a long (∼30 d) rise to the main peak. It is the first spectroscopically-normal double-peaked SN Ic to be observed. Our aim is to determine the properties of this explosion and of its progenitor star.
Methods. Optical photometry and spectroscopy of iPTF15dtg was obtained with multiple telescopes. The resulting light curves and spectral sequence are analyzed and modeled with hydrodynamical and analytical models, with particular focus on the early emission.
Results. iPTF15dtg is a slow rising SN Ic, similar to SN 2011bm. Hydrodynamical modeling of the bolometric properties reveals a large ejecta mass (∼10 $M_{\odot}$) and strong ^{56}Ni mixing. The luminous early emission can be reproduced if we account for the presence of an extended ($\gtrsim$500 $R_{\odot}$), low-mass ($\gtrsim$0.045 $M_{\odot}$) envelope around the progenitor star. Alternative scenarios for the early peak, such as the interaction with a companion, a shock-breakout (SBO) cooling tail from the progenitor surface, or a magnetar-driven SBO are not favored.
Conclusions. The large ejecta mass and the presence of H- and He-free extended material around the star suggest that the progenitor of iPTF15dtg was a massive ($\gtrsim$35 $M_{\odot}$) WR star that experienced strong mass loss.

Key words. supernovae: general

1. Introduction

Stripped-envelope (SE) supernovae (SNe) stem from the core-collapse of massive stars whose outer layers were removed. SNe IIb and Ib present little or no signatures of hydrogen but their spectra are helium rich. The spectra of SNe Ic are also helium-poor (e.g., Filippenko 1997).

SNe Ic exhibit fast-rising light curves (∼2 weeks) which are powered by ^{56}Ni at peak. The peak is followed by a relatively rapid decline, and the nebular phase starts at ∼2 months. Typical expansion velocities of normal SNe Ic are on the order of $\lesssim$10 000 km s^{-1}. There are SNe Ic with faster ejecta, which are sometimes associated with long-duration gamma-ray bursts (GRB; Woosley & Bloom 2006). These are known as broad-lined SNe Ic (SNe Ic-BL).

Well observed SNe Ic include, among others, SN 1994I (Filippenko et al. 1995), SN 2004aw (Taubenberger et al. 2006) and SN 2007gr (Valenti et al. 2008a). Drout et al. (2011) present a first multi-band sample of SNe Ic, Taddia et al. (2015a) present the sample of SNe Ic from SDSS and Bianco et al. (2014) and Modjaz et al. (2014) present the light curves and the spectra of 64/73 SE SNe obtained at the Harvard-Smithsonian Center for Astrophysics (CfA). Cano (2013), Lyman et al. (2016), and Prentice et al. (2016) have recently collected the known objects from the literature.

These investigations show that normal SN Ic ejecta are typically ≈2−4 $M_{\odot}$, energies are a few 10^{51} erg, and the ejected ^{56}Ni masses are typically ∼0.15−0.2 $M_{\odot}$. An important exception is SN 2011bm (Valenti et al. 2012), which is characterized by very massive ejecta (7−17 $M_{\odot}$) as inferred from the modeling of its broad light curve. Valenti et al. (2012) suggest a 30−50 $M_{\odot}$ progenitor star for SN 2011bm, which is consistent with the idea that single Wolf-Rayet (WR) stars with $M_{\rm ZAMS} > 25$–30 $M_{\odot}$ and a massive stellar wind produce SNe Ic. The most massive stars often outshine all the other stars in a galaxy and are responsible for much of the heavy-element nucleosynthesis, so understanding the final fate of the most massive stars is essential. However, the relatively small ejecta mass derived for most SNe Ic discussed above suggests that many of these SNe come instead from binary systems where a companion star has stripped the H and

He envelopes from the SN progenitor star (Smartt 2009; Eldridge et al. 2013).

To understand the nature of the progenitor stars of SE SNe, it is important to study the very early supernova emission (first few days, as in the case of PTF10vgv presented by Corsi et al. 2012). The detection of an early peak can bring important information on the radius of the progenitor star (Piro & Nakar 2013), but also on the outer structure of the star, the degree of ^{56}Ni mixing, as well as the presence of a companion or a dense circumstellar material (CSM).

Some SE SNe, such as SN Ib 1999ex (Stritzinger et al. 2002), SN Ib 2008D (Soderberg et al. 2008; Malesani et al. 2009; Modjaz et al. 2009), SN Ib/IIb iPTF13bvn (Fremling et al. 2016), and many SNe IIb (e.g., SN 1993J, Richmond et al. 1994; SN 2011dh, Arcavi et al. 2011; Ergon et al. 2014), do show this kind of early emission. The type Ib/c SN 2013ge showed an early peak but only in the ultra-violet (UV) light curves (Drout et al. 2016). For SN 2008D, the early peak in the optical has been explained by different scenarios: as a result of the presence of ^{56}Ni in the outermost layers or as the consequence of a modified density structure within the helium progenitor star (Bersten et al. 2013); as a shock-breakout (Rabinak & Waxman 2011); or as the effect of a jet in the explosion (Mazzali et al. 2008). A double peak was observed also for the peculiar SN Ib 2005bf (e.g., Folatelli et al. 2006) although, in this case, it is characterized by a longer timescale (~2 weeks past explosion, consistent with the explosion of a normal SE SN). A magnetar was invoked to explain the second peak and the late emission of SN 2005bf (Maeda et al. 2007). For SNe IIb, the shock breakout cooling tail for a relatively large progenitor radius (a few hundred solar radii) has been proposed as the powering mechanism of this early emission. This is the way to probe the radius of the progenitor stars for these SNe. For normal SNe Ic, we have hitherto not observed any early-time peak.

Superluminous SNe (SLSNe) Ic also show double-peaked light curves (Leloudas et al. 2012; Nicholl et al. 2015a; Nicholl & Smartt 2016). SLSNe are very luminous ($M_R < -21$ mag) transients, probably arising from the explosion of very massive star (Quimby et al. 2011; Gal-Yam 2012). In this case, it has been proposed that the first peak is powered by the post-shock cooling of extended stellar material (Nicholl et al. 2015a; Piro 2015), whereas the main peak could be powered by a magnetar. Kasen et al. (2016) suggest that the first peak seen in SLSNe could also be a signature of a central magnetar, whose energy inflates a bubble that drives a shock through the SN ejecta.

Finally, some SNe Ic-BL connected to GRBs have also shown early emission owing to the presence of a luminous GRB afterglow (e.g., SN 2013dx, D'Elia et al. 2015). SN 2006aj, a SN Ic-BL associated with an X-ray flash (e.g., Sollerman et al. 2006), also showed a double peak. The early maximum was interpreted as being due to the presence of an extended envelope formed by a dense wind (Campana et al. 2006; Waxman et al. 2007; Irwin & Chevalier 2016). Similar to SN 2006aj, the GRB-SN 2010bh also exhibited an early peak (Cano et al. 2011). The shock break-out through an extended and low-mass envelope could power the early peak (Margutti et al. 2015; Nakar 2015).

In this paper, we present iPTF15dtg, the first spectroscopically normal SN Ic with a detected double peak in the optical light curves. Through the analysis of the SN light curves, we estimate progenitor and explosion properties that are consistent with the core collapse of a massive WR star that suffered strong mass loss prior to its explosion.

The paper is structured as follows: in Sect. 2, we present the observations and how the data were reduced; in Sect. 3, we discuss the host galaxy. Section 4 shows the SN light curves, and Sect. 5 presents the SN spectra. In Sect. 6, we analyze and model the SN data. The results from the analysis are discussed in Sect. 7, and our conclusions are given in Sect. 8.

2. Observations and data reduction

Supernova iPTF15dtg was discovered on JD 2 457 333.931 at $g = 19.63 \pm 0.16$ mag at RA = 02:30:20.05 and Dec = +37:14:06.7 (J2000.0) on an image taken using the 48-inch Samuel Oschin telescope (P48) at Palomar Observatory, equipped with the 96 Mpixel mosaic camera CFH12K (Rahmer et al. 2008). The SN was not detected on JD 2457332.933 or JD 2 457 332.965 (i.e., 0.966 days before discovery) at limiting magnitude $g \geq 20.46$ mag and 20.16 mag, respectively. In the following, we adopt the average between the epochs of last non-detection and discovery as the explosion date ($t_{\rm explo}$ = JD 2 457 333.448 ± 0.483), unless specified differently. Times are given with respect to this date in the observer's frame throughout the paper, unless otherwise specified.

We followed the SN with the P48 in the g-band until ~100 d after discovery. P48 photometry was reduced with the Palomar Transient Factory Image Differencing and Extraction (PTFIDE) Pipeline[1,2], which performs template subtraction and PSF photometry.

We also obtained photometry with the Palomar 60-inch telescope (P60; Cenko et al. 2006) in the *Bgri*-bands, starting 2 d after discovery (B-band coverage started from +4.5 d). We furthermore used the Nordic Optical Telescope (NOT; Djupvik & Andersen 2010) to monitor the SN in *gri* during the post-peak phase. The last images were obtained ~130 days after explosion with the NOT. In Fig. 1, we show iPTF15dtg in its host galaxy, in a g-band image taken on Jan. 10 2016 with the NOT. P60 and NOT photometric data were reduced using the pipeline presented in Fremling et al. (2016). In Table A.1 we report a log of the photometric observations. As reference stars to calibrate the P60 photometry, we used 14 stars in the SN field which were, in turn, calibrated using a Sloan Digital Sky Survey (SDSS; Ahn et al. 2014) field observed at similar airmass. The final light curves are presented after combining the magnitudes obtained the same night.

Ten optical spectra were obtained from +3 d until +123 d, using the Telescopio Nazionale Galileo (TNG) + DOLoRes, the Keck + the Low Resolution Imaging Spectrometer (LRIS; Oke et al. 1995), the NOT + the Andalusia Faint Object Spectrograph and Camera (ALFOSC), the Discovery Channel Telescope (DCT) + the DeVeny spectrograph + the Large Monolithic Imager (LMI), and the Gemini North telescope + GMOS. The spectra were reduced in the standard manner, including wavelength calibration using an arc lamp, and flux calibration using a standard star (for each telescope, we made use of dedicated pipelines, as in Fremling et al. 2016). In Table A.2, we report our spectral log.

We also observed iPTF15dtg with the Karl G. Jansky Very Large Array (VLA; Perley et al. 2011) under our Target of Opportunity program[3]. The first observation was carried out on Dec. 17 2015 (+40 d), between 00:28:40 and 01:28:30 UT,

[1] http://spider.ipac.caltech.edu/staff/fmasci/home/miscscience/ptfide-v4.5.pdf
[2] http://web.ipac.caltech.edu/staff/fmasci/home/miscscience/forcedphot.pdf
[3] VLA/15A-314; PI: A. Corsi.

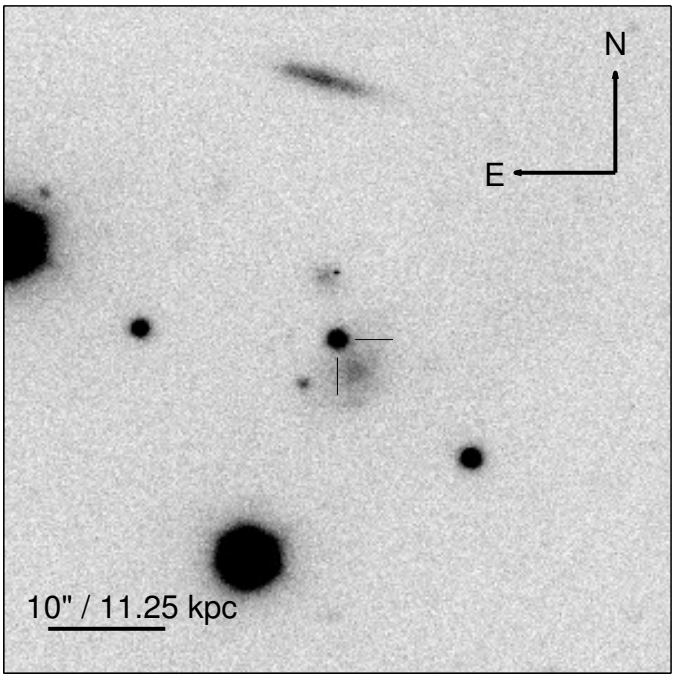

Fig. 1. iPTF15dtg (indicated by two black segments) and its host galaxy in a *g*-band frame taken at the NOT on Jan. 10 2016 with ALFOSC. The orientation of the image is indicated in the top-right corner, whereas the scale is shown in the bottom-left.

with the VLA in its D configuration. A second observation was carried out on Jan. 7 2016 (+61 d), between 03:35:58 and 04:35:41 UT, with the VLA in its DnC configuration. VLA data were reduced and imaged using the Common Astronomy Software Applications (CASA) package. Both observations yielded non-detections. We thus set the following 3σ upper-limits on iPTF15dtg radio flux: $\lesssim$23 μJy at 6.4 GHz during the first epoch, and $\lesssim$20 μJy at 6.2 GHz during the second epoch.

3. Host galaxy

Supernova iPTF15dtg was located in an anonymous galaxy at redshift $z = 0.0524 \pm 0.0002$, which corresponds to a luminosity distance $D_L = 232.0$ Mpc and distance modulus $\mu = 36.83$ mag. Here we assumed WMAP 5-years cosmological parameters ($H_0 = 70.5$ km s^{-1} Mpc^{-1}, $\Omega_M = 0.27$, $\Omega_M = 0.73$, Komatsu et al. 2009). The redshift was determined from the Gaussian fit of some of the host-galaxy emission lines (Hα, Hβ, [O III] λ5007) superimposed on the SN spectra (see Sect. 5).

We assume that no host extinction affects the emission of iPTF15dtg, as we do not detect any narrow Na I D absorption lines at the host-galaxy rest wavelength. The Milky Way extinction in the *Bgri*-bands is $A_B = 0.235$ mag, $A_g = 0.214$ mag, $A_r = 0.148$ mag, and $A_i = 0.110$ mag (Schlafly & Finkbeiner 2011).

The host galaxy has integrated magnitudes of $M_g = -17.4$ mag, $M_r = -17.8$ mag, and $M_i = -17.9$ mag. This corresponds to a global metallicity of 12+log(O/H) = 8.29 ($Z/Z_\odot = 0.39$) following the luminosity-color-metallicity relation by Sanders et al. (2013), or $Z/Z_\odot = 0.32$ using the luminosity-metallicty relation by Arcavi et al. (2010). From the SN spectrum taken on Dec. 6 2015, we could measure the emission line fluxes of the host galaxy at the exact SN position. Based on their flux ratios, we derived a metallicity of 12+log(O/H) = 8.22 ± 0.20 ($Z/Z_\odot = 0.34$) at the SN location using the O3N2 calibration by Pettini & Pagel (2004). The inferred metallicity at the location of iPTF15dtg is lower than that found for most of the other normal SNe Ic (Sanders et al. 2012) and more similar to the metallicities for SNe from blue supergiant stars, SLSNe, and SN impostors (Taddia et al. 2013, 2015b; Lunnan et al. 2014). The natal metallicity of iPTF15dtg appears to be comparable with that of long-duration GRBs (Krühler et al. 2015 find a range of host metallicities of 12+log(O/H) = 7.9–9.0, with a median of 8.5).

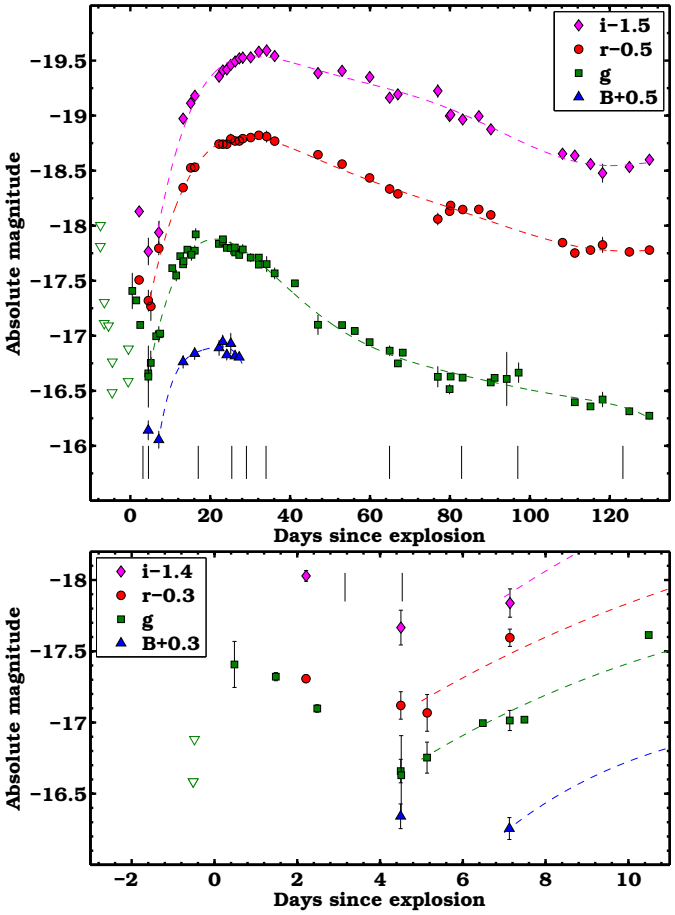

Fig. 2. *Top panel*: *Bgri* absolute-magnitude light curves of iPTF15dtg from P48, P60, and NOT. The main peak is fit by low-order polynomials, shown as dashed lines. The epochs of spectral observations are indicated by vertical black segments. Pre-explosion magnitude limits in the *g*-band are indicated by triangles. In the *gri* filters, we notice the presence of an early peak, unprecented among spectroscopically normal SNe Ic. *Bottom panel*: the early *Bgri* light curves of iPTF15dtg.

4. Light curves

In Fig. 2, we present the *Bgri* light curves of iPTF15dtg. The *g*-band emission exhibits an early peak at −17.4 mag, followed by a declining phase lasting for about four days (see the bottom panel). Also the *r* and *i*-bands show this early declining phase. In the *B*-band, we detect only one epoch on the early declining phase since the observations in this filter began a few days later.

This early declining phase has been observed in other SE-SNe and in SLSNe, as shown in the top panel of Fig. 3. Here we compare the absolute magnitudes of the early phase of iPTF15dtg to those of four other SNe belonging to different types and exhibiting a double-peaked light curve. The early peak of iPTF15dtg in the *g*-band has a timescale similar to that of

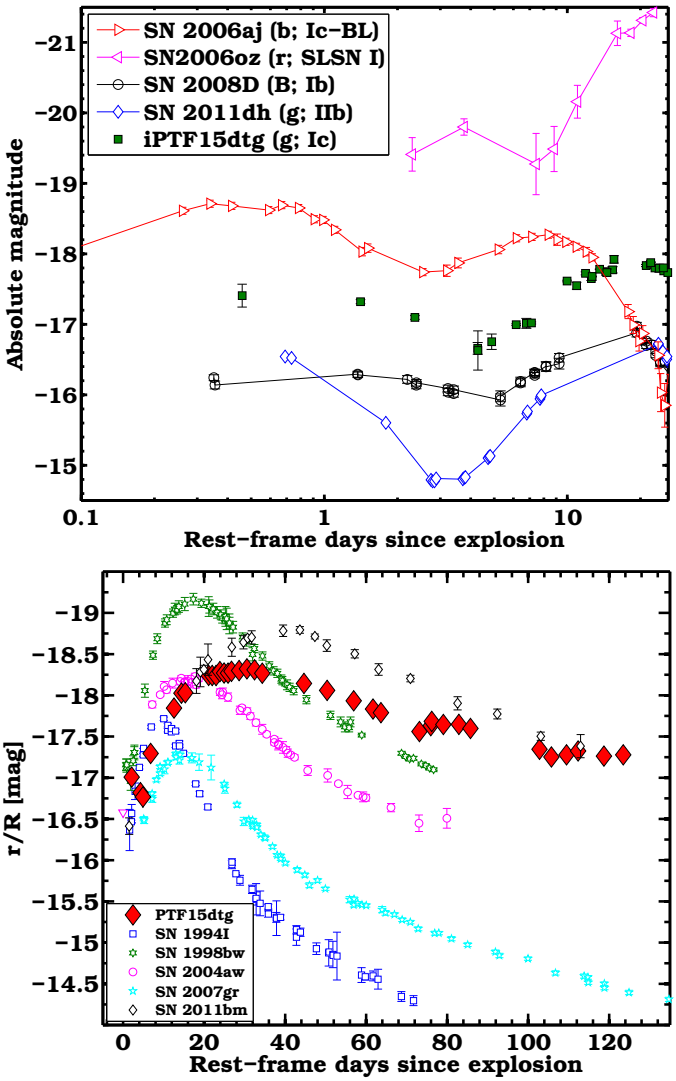

Fig. 3. *Top panel*: comparison of the early g-band light curve of iPTF15dtg to the early light curves of other SE SNe and SLSNe that exhibit a double peak. For each SN the filter and the SN type is reported in the legend. The data for SNe 2006aj, 2006oz, 2008D, and 2011dh are taken from Brown et al. (2009), Leloudas et al. (2012), Bianco et al. (2014), and Arcavi et al. (2011), respectively. *Bottom panel*: absolute r-band magnitudes of iPTF15dtg compared to those of other well-studied SNe Ic from the literature. Data for SNe 1994I, 1998bw, 2004aw, 2007gr, 2011bm are from Richmond et al. (1996), Clocchiatti et al. (2011), Taubenberger et al. (2006), Hunter et al. (2009), Valenti et al. (2012), respectively.

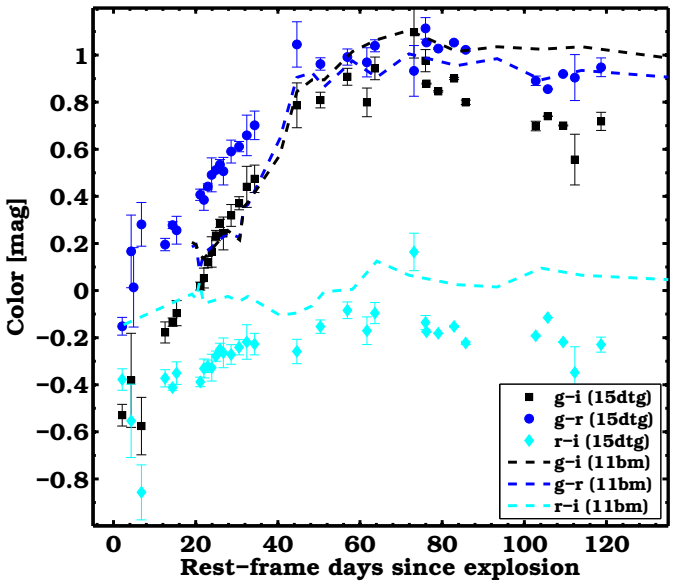

Fig. 4. Color evolution of iPTF15dtg ($g-r$, $g-i$, $r-i$) compared to that of SN 2011bm (Valenti et al. 2012).

the other events, whereas its luminosity is in-between those of SN Ic-BL 2006aj and SLSN 2006oz, and those of SN Ib 2008D and SN IIb 2011dh. After the first decline, all the light curves start to rise, reaching maximum (see top panel) at relatively late epochs for a SN Ic, namely at +22.6, +21.2, +28.7, and +30.9 days in B, g, r, and i, respectively (21.5, 20.1, 27.3, 29.4 days in the rest frame). We determined the maximum epochs by fitting the light curves by low order polynomials, indicated in Fig. 2 by dashed lines.

The light curves of iPTF15dtg are quite broad and are characterized by $\Delta m_{15} = 0.34$, 0.16, and 0.11 mag in g, r, and i, respectively (in the observer frame). The broadness of the light curves of iPTF15dtg is evident when we compare its r-band light curve with those of other well observed SNe Ic (see the bottom panel of Fig. 3). SN iPTF15dtg peaks later than any other SN Ic, with the exception of SN 2011bm. Also SN Ic 2010mb (Ben-Ami et al. 2014) shows a late peak, but that SN is characterized by strong emission lines in the spectra owing to the interaction with its CSM. On the other hand, iPTF15dtg ($M_r^{\rm max} = -18.3$ mag) is only slightly brighter than normal SNe Ic, such as SN 2007gr, with a peak similar to that of SN 2004aw and slightly fainter than SN 2011bm, but clearly fainter than a SN Ic-BL, such as SN 1998bw. The r-band decline rate of iPTF15dtg at $\gtrsim$+80 d is slower than that of the other SNe Ic, including SN 2011bm.

The color evolution of iPTF15dtg is shown in Fig. 4. The fast cooling in the early phase is clearly visible in the $g-i$ color. Thereafter all the colors show a slower trend to the red, until ~50 days when they are flatter. The color evolution of iPTF15dtg is very similar to that of SN 2011bm. For iPTF15dtg $g-r$ is redder at pre-peak epochs (before ~40 d), $g-i$ is bluer at later epochs, $r-i$ is bluer at all epochs.

5. Spectra

SN iPTF15dtg was spectroscopically followed from +3 d until +123 d. The spectral sequence is shown in Fig. 5. All the spectra will be released via WISeREP (Yaron & Gal-Yam 2012). The initially blue almost featureless spectrum is followed by a progressive reddening with the characteristic lines of a SN Ic emerging from the continuum. No H or He lines are detected. The spectra are dominated by Ca, O, and Fe lines. Ca II and O I characterize the red part of the spectrum, with broad P-Cygni profiles. Fe II λ5169 is visible after +17 d, Na I D emerges at ~+60 days, and [O I] λ5577, [O I] λ6300 at ~+80 d. In the first two spectra, C II features (at 6580 Å and 7234 Å) are also identified.

Figure 6 illustrates that the spectra of iPTF15dtg resemble those of SN 2004aw, and also those of SN 2011bm. The spectra show an almost identical pattern in the red part, owing to the P-Cygni profiles of Ca II and O I. These three SNe have spectra that also show three emission peaks in the blue part, at ~4000, 4800, 5500 Å, as well as Si II below the narrow Hα emission line from the host. The +123 d spectrum of iPTF15dtg is remarkably

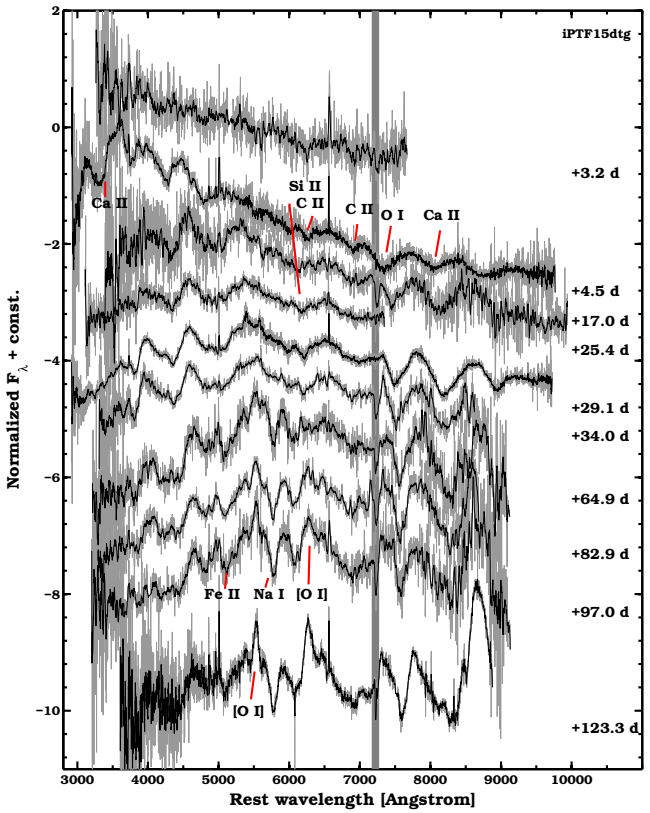

Fig. 5. Spectral sequence of iPTF15dtg. In gray, we show the unbinned spectra, in black the same spectra after smoothing. The spectra are normalized by their median and shifted vertically for clarity. The spectra are de-redshifted but they are not corrected for extinction. For each spectrum we report its phase (in days since explosion). The main telluric feature is indicated by a gray area. Line identifications are reported for some of the main features.

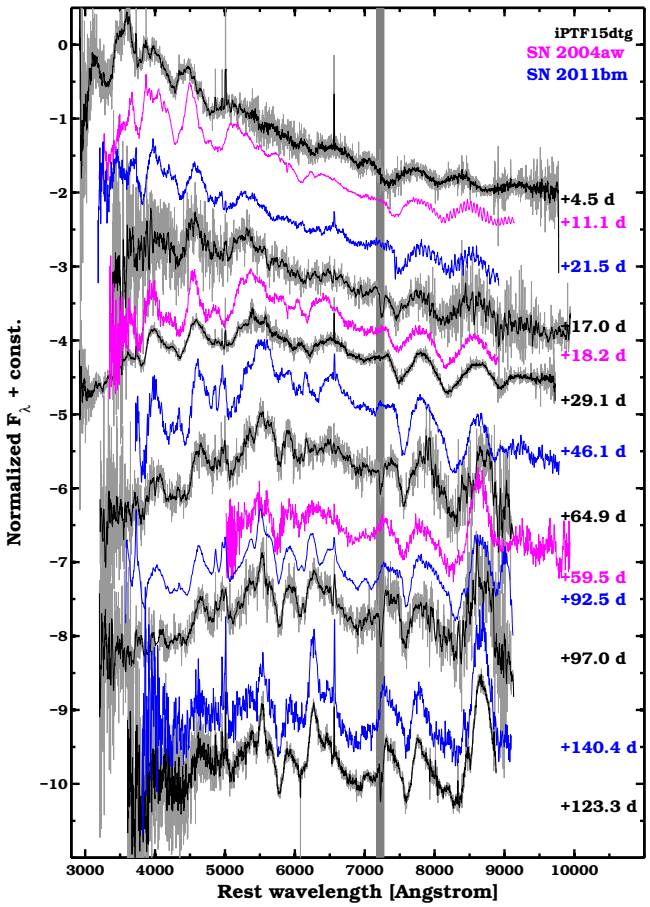

Fig. 6. Spectral comparison of iPTF15dtg to the SNe Ic 2004aw (Taubenberger et al. 2006) and 2011bm (Valenti et al. 2012). Each spectrum is corrected for redshift and extinction. Their phases are reported in days since explosion.

similar to that of SN 2011bm taken at a similar phase (+140 d), with both spectra exhibiting nebular features, in particular strong [O I] emission at 5577 Å and 6300 Å.

The spectral similarity between these SNe implies that the velocity evolution of the different lines are quite similar, in particular between iPTF15dtg and SN 2004aw, as shown in Fig. 7. Here we compare the velocities of Ca II, O I, and Si II, which we derived from the absorption minima of the P-Cygni profiles. We also report the velocities of Na I D and C II λ6580 for iPTF15dtg. For iPTF15dtg, we also measured the Fe II λ5169 velocities, which are used to model the SN bolometric light curve (see Sect. 6). These measured velocities are consistent with those of normal SNe Ic (Modjaz et al. 2016). All the line velocities decrease with time up to ∼30 d, thereafter they are almost constant.

6. Modeling

6.1. Bolometric properties

Using the *gri* light curves we build a quasi bolometric (L_{gri}) and a bolometric ($L_{\rm BB}$) light curve, shown in the top panel of Fig. 8. To obtain L_{gri} we linearly interpolate the light curves at the same epochs, we convert the extinction-corrected *gri* magnitudes into specific fluxes at the effective wavelength (Fukugita et al. 1996) of their filters, and integrate the resulting spectral energy distribution (SED). To build $L_{\rm BB}$, we fit a black-body (BB) function to the SED, to also account for the flux in the near-infrared (NIR) and in the UV. The fluxes obtained from the integrated SED and BB are multiplied by $4\pi D_L^2$, where D_L is the luminosity distance. We do not consider the *B*-band in our SED because it has a limited temporal coverage and because it could be affected by line blanketing.

As our SEDs do not include emission in the UV or in the NIR, we check if $L_{\rm BB}$ is consistent with the bolometric light curve ($L_{\rm Bol}$) that we derive using the bolometric corrections (BCs) for SE SNe presented by Lyman et al. (2014). We make use of the BCs to convert M_g and extinction-corrected $g-r$ into $L_{\rm Bol}$. For the first epoch we use the BC listed in Table 4 of Lyman et al. (2014), whereas for the remaining epochs we use those listed in their Table 2. The resulting $L_{\rm Bol}$ is shown in red diamonds in the top panel of Fig. 8. $L_{\rm Bol}$ turns out to be fainter than $L_{\rm BB}$, probably because of the line blanketing in the bluer part of the spectrum, which makes the actual SED less luminous than the best BB fit. Hereafter we use $L_{\rm Bol}$ obtained from the BCs of Lyman et al. (2014) as our bolometric light curve.

The BB fit on the SEDs gives us an estimate of the temperature (T), shown in the central panel of Fig. 8. It is clear that the ejecta are progressively cooling down. The cooling is particularly strong between the first and the second epoch, with T dropping from 1.5×10^4 K to 1.0×10^4 K in ∼2 days.

In the bottom panel of Fig. 8, we show the BB-velocity ($\rm Vel_{BB}$) as derived from the fit by dividing the resulting BB-radius by the time since explosion. The photosphere recedes in the slowest part of the ejecta as the time increases.

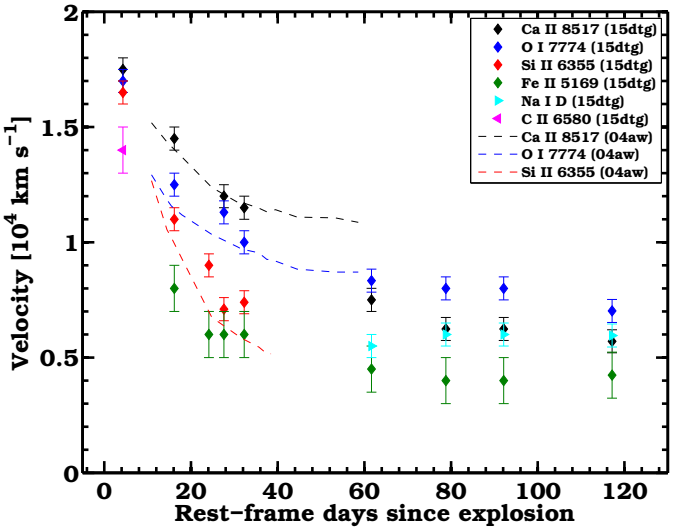

Fig. 7. P-Cygni minima velocities for different lines in the spectra of iPTF15dtg, as compared to those of SN 2004aw from Taubenberger et al. (2006).

6.2. Modeling of the main peak

6.2.1. Arnett model

To derive estimates of the ejecta mass ($M_{\rm ej}$), the ^{56}Ni mass, and the explosion energy (E_K) for iPTF15dtg, we can fit the main peak of the bolometric light curve and the photospheric velocity using a simple Arnett model (see e.g., Valenti et al. 2008b; Cano 2013; Taddia et al. 2015a). The model assumes constant opacity κ, which we set to 0.07 cm^2 g^{-1}. This value was also used by Cano (2013) and Taddia et al. (2015a), since it is appropriate for the electron scattering in H-poor SNe (the assumption of a constant opacity is obviously a limitation of this model, see e.g., Wheeler et al. 2015; and Dessart et al. 2016). The model also assumes that the ^{56}Ni is located at the center of the ejecta. We adopt the relation between E_K, $M_{\rm ej}$, and the photospheric velocity that is valid for a sphere of constant density, as in Taddia et al. (2015a). We use 6000 km s^{-1} as the photospheric velocity in the Arnett model, from the measured Fe II λ5169 P-Cygni minima (these values are shown as blue squares in the bottom panel of Fig. 8).

By fitting the model to the bolometric light curve, we obtain $E_K = (2.2 \pm 0.1) \times 10^{51}$ erg, $M_{\rm ej} = 10.3 \pm 0.6\ M_\odot$, and M(^{56}Ni) $= 0.42 \pm 0.01\ M_\odot$. The given uncertainties only include the errors of the fit. The ejecta mass thus obtained is substantially higher than that of normal SNe Ic. The ^{56}Ni mass to ejecta mass ratio (~0.04) is similar to that of other normal SNe Ic (Cano 2013), and provides a good argument for radioactive heating (and against magnetar heating). The model, shown by a thin dashed line in the top panel of Fig. 8, is overall able to reproduce the light curve with good accuracy, but it fails to provide a good fit at early epochs. The rise occurs later in the model, as a result of the centralized ^{56}Ni distribution.

6.2.2. Hydrodynamical model

Given the simplified assumptions in the Arnett model, we try to refine the estimates of the progenitor properties by making use of the Modules for Experiments in Stellar Astrophysics (MESA; Paxton et al. 2011) and of the SuperNova Explosion Code (SNEC; Morozova et al. 2015). MESA allows us to build a

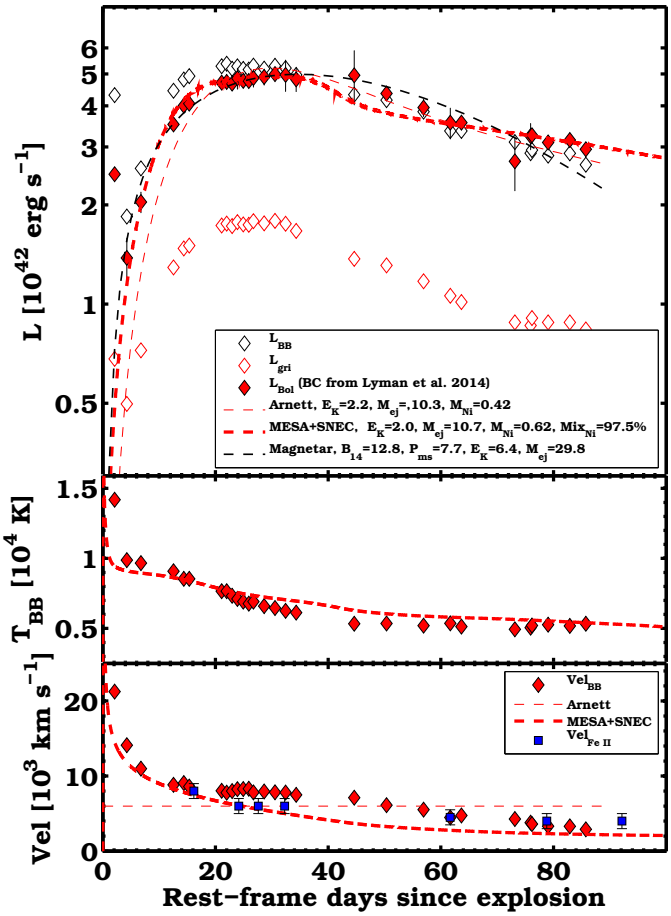

Fig. 8. *Top panel*: bolometric light curves of iPTF15dtg. The empty black diamonds represent the bolometric light curve obtained from the BB fit to the SEDs. The empty red diamonds represent the *gri* integrated luminosity. The filled red diamonds show the bolometric luminosity obtained using the bolometric corrections presented by Lyman et al. (2014). The best Arnett fit to this light curve is shown by a red dashed line. The best hydrodynamical model fit is shown by a thick dashed line. The best magnetar model is shown by a black dashed line. *Central panel*: BB-temperature evolution for iPTF15dtg, along with the temperature evolution of the best hydrodynamical model. *Bottom panel*: BB velocity (red diamonds) and Fe II velocities for iPTF15dtg. The best hydrodynamical model fit is shown by a thick dashed line, the velocity adopted for the Arnett model is represented by a thin dashed line, and fits the Fe II velocities around peak.

progenitor star via its stellar evolution code whereas, with the 1-dimensional (1D) hydrodynamical code SNEC, we can explode this progenitor and calculate a bolometric light curve.

Our approach is to construct a real stellar evolution and hydrodynamical model based on the input we have from the Arnett model fit to the SN data, without covering a large parameter space. We used MESA to obtain a star with a final mass of ~12 $M_\odot$, which implies an ejecta mass of ~10 $M_\odot$, as suggested by our Arnett model. We first set the metallicity of our stellar evolution model to $Z = 0.00676 = 0.34\ Z_\odot$, consistent with the metallicity measured from the host-galaxy emission lines in Sect. 3. Since we wanted to obtain a H-free progenitor (iPTF15dtg is a SN Ic), we focused on single stars with initial masses >30 $M_\odot$, which have the necessary mass-loss rate to expel the outer H layer. We also considered that massive stars can be characterized by rapid rotation. Given these boundary conditions, after running a series of models with MESA, we finally

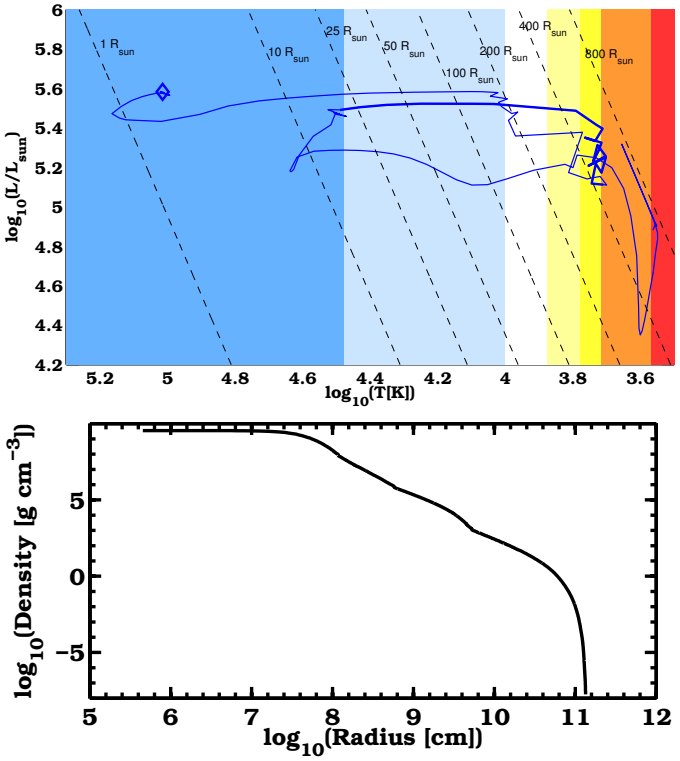

Fig. 9. *Top panel*: evolution of our MESA star model in the HR diagram. The position of the progenitor star just before collapse is marked by a blue diamond. This progenitor star has a compact radius (see dashed black lines) and it is characterized by a rather high temperature (10^5 K), therefore it belongs to the O stellar type. The phase when most of the H mass is lost owing to strong winds is shown by a thicker blue line. *Bottom panel*: density profile of our progenitor star model.

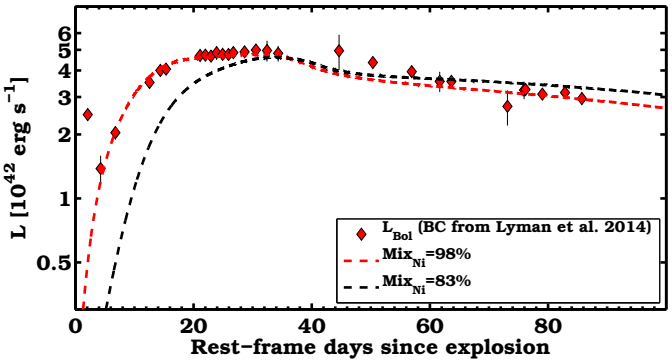

Fig. 10. Effect of ^{56}Ni mixing on the light curve models of iPTF15dtg. Almost full mixing (red dashed line) is required to fit the early rise and the main peak shape. Even a model with a value of 83% for ^{56}Ni mixing (black dashed line) does not fit the early rise.

produced a 12.1 $M_\odot$ H-free star, with a radius of ∼1.9 $R_\odot$, and a surface temperature of 10^5 K, that is consistent with a massive WR star. This star has a total helium mass of 4.96 $M_\odot$. To produce this result, we evolved a star with an initial mass of $M_{\rm ZAMS}$ = 35 $M_\odot$, rotating at $v_{\rm surf}$ = 105 km s^{-1}. The evolution in the Hertzsprung-Russell (HR) diagram of this star up to collapse is shown in the top panel of Fig. 9. The density profile of the progenitor star is shown in the bottom panel. Most of the H envelope is lost owing to strong winds (the mass-loss rate reaches a peak of $\sim 1.3 \times 10^{-1}$ $M_\odot$ yr^{-1}) when the star is about 5.3×10^6 yr old.

We exploded this 12.1 $M_\odot$ H-free star leaving 10.7 $M_\odot$ in the ejecta, with an explosion energy of 2×10^{51} erg (as inferred from the Arnett model). These values allowed us to reproduce the Fe II λ5169 velocity profile of iPTF15dtg (see bottom panel of Fig. 8).

As the Arnett model does not assume any ^{56}Ni mixing, and thus fails to reproduce the early rise to the main peak of the light curve, we resorted to uniformly distribute the ^{56}Ni up to the outer layers of the SN. After a few attempts, we found that by mixing the ^{56}Ni out to 97.5% of the progenitor mass, the hydrodynamical model nicely fits the rise and the flat peak of the bolometric light curve, as well as the declining phase. In Fig. 10 we show how a lower degree of mixing (83%) fail to reproduce the early rise and the peak shape.

We chose a ^{56}Ni mass of 0.62 $M_\odot$. This was higher than the estimate from the Arnett model (this difference is mainly due to the mixing) but it allowed us to fit the SN peak with the hydrodynamical model. This is shown in Fig. 8 (top-panel).

The MESA+SNEC model also fits the temperature evolution, as shown in the central panel of Fig. 8.

Neither the best hydrodynamical model nor the Arnett model can reproduce the early peak. In Sect. 6.3, we make use of the parameters obtained for the ejecta mass and the explosion energy as input for other models, which include the physics needed to explain the luminous early peak.

6.2.3. Magnetar model

There is also the possibility that the main peak is powered by a magnetar (see e.g., Maeda et al. 2007, for SN 2005bf). This mechanism has been suggested for superluminous supernovae (Kasen & Bildsten 2010). We fit the magnetar model by Kasen & Bildsten (2010, see also Inserra et al. 2013) to the bolometric light curve and to the Fe II velocity at the epoch of maximum, obtaining E_K = (6.4 ± 0.5)×10^{51} erg, $M_{\rm ej}$ = 29.8 ± 2.2 $M_\odot$, B = (12.8 ± 0.4)× 10^{14} G, and P = 7.7 ± 0.6 ms. Here B is the magnetic flux density, P is the rotation period of the magnetar. The model does reproduce the light curve (black dashed line in Fig. 8), but not as well as the hydrodynamical radioactively-powered model, especially on the declining phase. Moreover, this SN is not superluminous and its spectra do not show features associated with the presence of a magnetar, therefore we disfavor this scenario.

6.3. Modeling of the early peak

The early (∼3 d) peak in the light curves of iPTF15dtg is the first one ever observed for a spectroscopically normal SN Ic. There are different scenarios that can potentially explain the presence of this feature and, in the following, we discuss each of them.

Possible mechanisms are: 1) the shock breakout cooling (SBO) tail (e.g., Piro & Nakar 2013); 2) the emission from interaction with a companion star (Kasen 2010); 3) a magnetar-driven SBO (Kasen et al. 2016); 4) the emission from a progenitor star surrounded by an extended envelope of relatively small mass (Nakar & Piro 2014; Piro 2015; Margutti et al. 2015; Nakar 2015).

Each of these models depends on several parameters whose degeneracy is impossible to break by just fitting the early peak. Therefore, we make use of the results derived from the hydrodynamical modeling of the main peak and fix some of the parameters to the values derived there (in Sect. 7, we discuss some caveats related to the hydrodynamical modeling). In particular

we adopt the explosion energy and ejecta mass from Sect. 6.2.2. Whereas this approach does not provide a fully consistent model of the entire bolometric light curve, it allows us to reduce the degree of freedom and provide good estimates on the parameters that only the early emission can constrain. The modeling in the following sections demonstrates that the only favourable scenario is the extended-envelope model.

6.3.1. The shock-break-out cooling-tail scenario

The SBO scenario seems inconsistent with a small progenitor radius, like the one of the progenitor star we exploded to fit the main peak. Indeed, in Fig. 8, the early peak in the bolometric light curve is not fitted by the best hydrodynamical model. We use the analytic model from Piro & Nakar (2013) to further test the SBO cooling tail model. In their Eqs. (1) and (2), Piro & Nakar (2013) provide expressions for the luminosity and the temperature as a function of time. Assuming BB emission, we can derive the luminosity in the *Bgri*-bands to directly compare with the observed data. In the model by Piro & Nakar (2013), we use the explosion energy and the ejecta mass obtained in Sect. 6.2 from the hydrodynamical model of the bolometric light curve ($M_{\rm ej} = 10.7\ M_{\odot}$, $E_K = 2.0 \times 10^{51}$ erg). We also adopt $\kappa = 0.2$ cm^2 g^{-1}, since we assume that the H-free gas is fully ionized at this stage. The explosion epoch is again assumed to be the average of last non-detection epoch and discovery epoch (the uncertainty is only ~0.5 d). Then, we solve for the only variable that is left, which is the progenitor radius. It turns out that it is not possible to provide a good fit of the early emission since the large ejecta mass implies a timescale for the cooling that is longer than the observed one. If we match the early peak *g*-band magnitude, we would obtain a large radius of ~500 $R_{\odot}$, but the model clearly does not fit (see Fig. 11, where the SBO model in *Bgri*-bands for $R = 510\ R_{\odot}$ is indicated by dashed lines). We therefore exclude a SBO cooling tail model for iPTF15dtg.

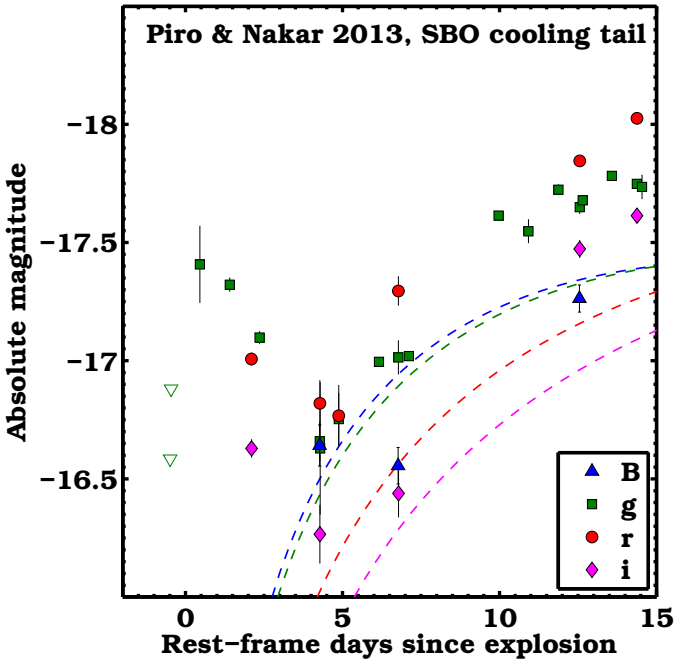

Fig. 11. Piro & Nakar (2013) model (dashed lines) for the early light curve of iPTF15dtg, in *Bgri*-bands. In the modeling, we adopt the ejecta mass and explosion energy derived from the hydrodynamical modeling. The large ejecta mass implies a long timescale for the cooling tail in the optical, which cannot reproduce the early peak of iPTF15dtg.

6.3.2. The companion-interaction scenario

In this section we try to test if the early emission can arise from the interaction between the SN ejecta and a putative companion star, as described in the model by Kasen (2010). We set the inner and the outer ejecta density profiles to be power laws of the radius ($\rho \propto r^{-\delta}$ and $\rho \propto r^{-n}$) with $\delta = 0$ and $n = 6$, which is appropriate for a compact progenitor star (Chevalier 1982). As in the SBO cooling-tail model, we adopt $M_{\rm ej} = 10.7\ M_{\odot}$, $E_K = 2.0 \times 10^{51}$ erg and $\kappa = 0.2$ cm^2 g^{-1}. The free parameters left are the binary separation, *a*, and the explosion epoch (which is however constrained by the good pre-discovery limits). If we fit the first five days in the light curves, neglecting the ^{56}Ni contribution, then the Kasen (2010) model provides a good fit to at least the *B*, *g*, and the *r*-band, as shown by the dashed lines in Fig. 12. The *i*-band flux is overestimated. The best fit is obtained for a binary separation of 190 $R_{\odot}$, and for an explosion epoch coincident with the last non-detection. We note that for larger values of the index *n*, the quality of the fit is worse. However, the ^{56}Ni contribution is also important in the first days since our best hydrodynamical model shows that the ^{56}Ni is mixed out into the outer layers. A strong ^{56}Ni mixing allowed us to fit the rise to the main peak and its flat shape. In Fig. 12 the emission from the ^{56}Ni, as derived from the hydrodynamical model (assuming BB emission), is represented by dotted lines in the *Bgri*-bands. If we sum the companion interaction emission and the ^{56}Ni contribution, the total emission of the model (solid lines) is clearly in excess compared to the data in all the bands already at three days. This model might still work if we allow for a lower degree of ^{56}Ni mixing. If we distribute the ^{56}Ni up to 83% of the progenitor mass instead of 97%, we can get a good fit for the first five days in the *B* and *g*-bands (and a reasonable fit to the *r*-band, but not in the *i*-band). However, we would strongly underestimate the flux in all the bands on the rise to the main peak. A strong ^{56}Ni mixing thus seems to be necessary to fit the bolometric light curve rise, and makes it difficult to find a good fit for the Kasen (2010) model. The transition between the first peak and the rise to the main peak is clearly sharper in the observed data than in the model shown by the solid lines in Fig. 12, and thus the mechanism powering the main peak must have a timescale that is even shorter than the one of the Kasen (2010) model, in all the bands. This is also true for other values of binary separation.

We also emphasise that the last spectrum of iPTF15dtg reveals a strong [O I] λ6300 line that is similar to that of SN 2011bm, for which a massive, and thus probably single progenitor system, was suggested (Valenti et al. 2012).

6.3.3. The magnetar-driven shock-break-out cooling-tail

Kasen et al. (2016) have recently shown that a magnetar-driven SBO could produce an early peak in a magnetar powered SN. If we use the magnetar parameters from Sect. 6.2, and modify the energy injected by the magnetar in the SN ejecta using Eqs. (26) and (27) in Kasen et al. (2016), we cannot simultaneously fit the time and the luminosity of the early peak of iPTF15dtg. Adopting a large (6×10^{52} erg) magnetar energy, we can fit the epoch of the early peak, but the luminosity of this model turns out to be almost ten times brighter, compared to the data. Also for this reason, we do not favor the magnetar scenario as the main powering source of iPTF15dtg.

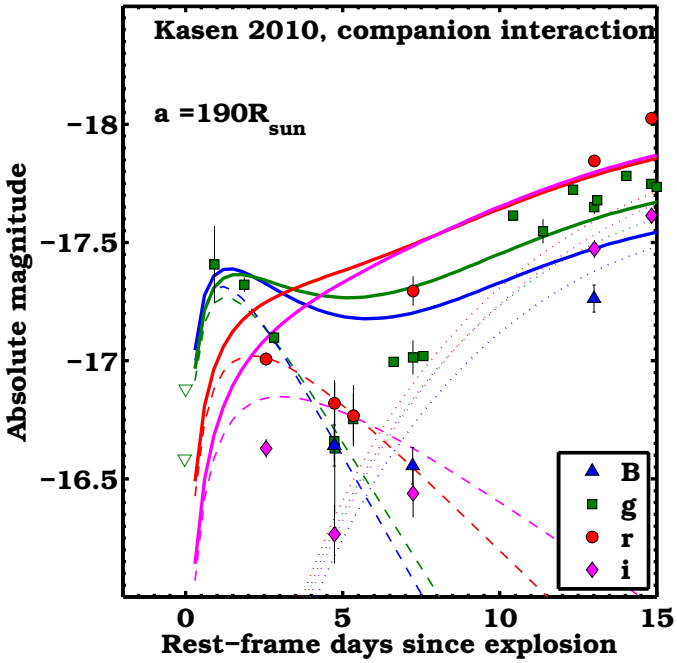

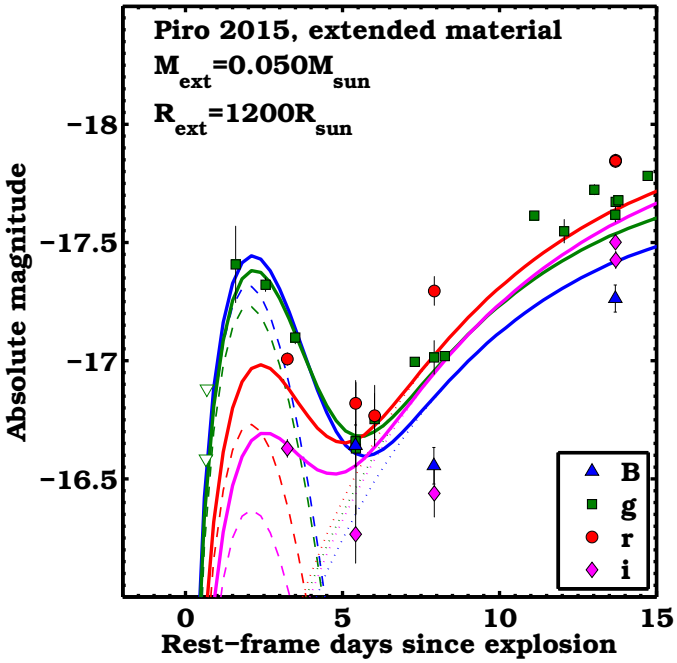

Fig. 12. Kasen (2010) model (dashed lines) for the early light curve of iPTF15dtg, in *Bgri*-bands. This model describes the emission from the interaction with a companion star. In the modeling, we adopt the ejecta mass and explosion energy derived from the hydrodynamical modeling. We modified the original Kasen (2010), optimized for SNe Ia, to reproduce the interaction of a compact WR star with a companion. Shown by dotted lines is the *Bgri* emission from the ^{56}Ni contribution, as derived from the hydrodynamical modeling. The Kasen (2010) model alone reproduces the *B*, *g*, and *r*-band emission up to +5 d. However, if we also add the ^{56}Ni contribution to the model, then there is a mismatch to the data owing to the long timescale of the companion interaction process.

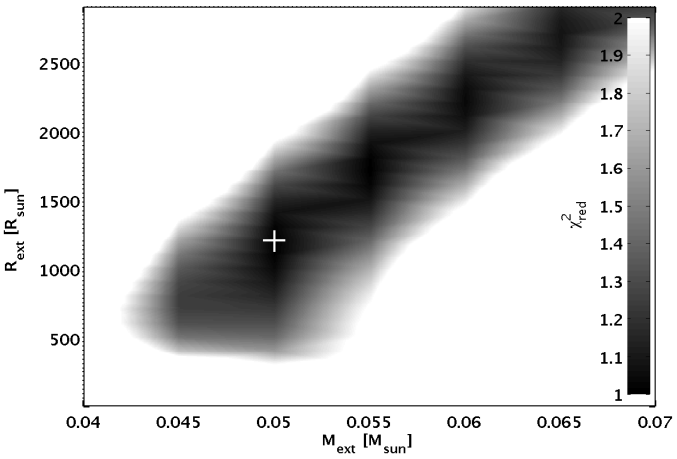

Fig. 13. *Top-panel*: Piro (2015) model (dashed lines) for the early light curve of iPTF15dtg, in *Bgri*-bands. This model describes the emission from a star surrounded by extended material and it has been constructed to reproduce double-peaked SNe. In the modeling, we adopt the ejecta mass and explosion energy derived from the hydrodynamical modeling. Shown by dotted lines is the *Bgri* emission from the ^{56}Ni contribution, as derived from the hydrodynamical modeling. The sum of the Piro (2015) model with the ^{56}Ni contribution provides a good match to the early peak, as well as to the rise to the main peak. This is due to the short timescale of the emission from the extended envelope. *Bottom-panel*: reduced χ^2 surface plot for the Piro (2015) model fit, given different values of $R_{\rm ext}$ and $M_{\rm ext}$, for the explosion epoch derived from the best fit. The best $R_{\rm ext}$ and $M_{\rm ext}$ fit values are indicated by a white cross. There is a clear degeneracy in the model fit for $R_{\rm ext} \gtrsim 500\ R_\odot$, and $M_{\rm ext} \gtrsim 0.045$.

6.3.4. The extended-envelope scenario

We can obtain a good fit to the early emission for all the bands using the double-peaked model by Piro (2015), which assumes that the progenitor star is surrounded by a low-mass, extended envelope. This could be in equilibrium, or mass ejected by the star during its life. In Fig. 13 the best fit is shown with colored solid lines, given by the sum of the Piro (2015) model (dashed lines) plus the ^{56}Ni contribution (dotted lines). For the Piro (2015) model we have three independent free parameters, namely the extension of the low mass envelope ($R_{\rm ext}$), its mass ($M_{\rm ext}$), and the explosion epoch. We assumed the same opacity, ejecta mass and energy as in the previous models. The model can reproduce the timescale of the first peak, as well as the luminosity in the different bands (with the exception of the *i*-band at five days). The best fit implies $R_{\rm ext} = 1200\ R_\odot$, $M_{\rm ext} = 0.05\ M_\odot$ and an explosion epoch occurring 0.7 observer-frame days before the last-non detection, since this is deep enough only to catch an emission brighter than −16.5 mag in the *g*-band.

There is a degeneracy between the two parameters $M_{\rm ext}$ and $R_{\rm ext}$, as shown in the bottom panel of Fig. 13. From this plot, we can conclude that around the progenitor of iPTF15dtg there was an envelope with a radius of at least $\gtrsim$500 $R_\odot$ and with a mass of $\gtrsim$0.045 $M_\odot$. We note that for SN IIb 2013cu (iPTF13ast, Gal-Yam et al. 2014) the wind/envelope radius was estimated as being $\gtrsim$720 $R_\odot$, similar to our object.

7. Discussion

Based on the fits of the early light curve, we favored the extended envelope scenario over the interaction with a companion star. The interaction scenario is also disfavored by the first two spectra, which show no interaction signatures. These spectra were taken before +5 d, when the early decline would still be powered by this interaction. Relatively broad lines arising from

the ejecta region where the reverse shock is propagating after the interaction with the companion should be visible in the high signal-to-noise spectrum taken with the Keck I telescope. We could also see narrow lines arising from the companion wind. However, the SN spectrum looks just like a normal SN Ic spectrum and the observed narrow lines are from the host galaxy.

We also considered the possibility that the early peak of iPTF15dtg was the result of an afterglow following a GRB or X-ray flash. However, the early spectrum does not resemble the afterglow spectra observed for GRB SNe. Furthermore, our radio upper limits constrain the 6 GHz radio flux of this SN as being $\leq 2 \times 10^{27}$ erg s^{-1} Hz^{-1}. This is an order of magnitude fainter that the emission from the GRB-associated SN 1998bw (Kulkarni et al. 1998) at comparable epochs (40–60 d since explosion). Following Valenti et al. (2008b), we used the interplanetary network (IPN) to search for a possible GRB association[4] in the interval between last non-detection and discovery, and we did not find any GRB detection. The same result was obtained considering a longer time interval, starting two days before the last non-detection.

As mentioned in the introduction, SN Ic-BL 2006aj was associated with an X-ray flash and showed an early declining phase, which was interpreted as the signature of an extended envelope, as in the case of iTPF15dtg. Furthermore, the metallicity at the location of iPTF15dtg is compatible with those of long-duration GRBs and the ejecta mass and ^{56}Ni mass of iPTF15dtg are in agreement with GRB-SNe (Cano et al. 2016). However, iPTF15dtg also shows clear differences from SNe Ic-BL associated to GRBs. More specifically, the main differences between iPTF15dtg and GRB-SNe are: (i) the kinetic energy is too low for a typical GRB-SN (even though Mazzali et al. 2006 find $E_K = 2 \times 10^{51}$ erg for SN 2006aj, similar to what we find here). (ii) No broad lines are observed in the optical spectra of iPTF15dtg and this certainly implies a normal Type Ic. However, we note that there was also a GRB-SN for which the features were not very broad (GRB 130215A/SN 2013ez; Cano et al. 2014), with derived line velocities comparable to those of normal SNe Ic (4000–6000 km s^{-1} near peak light) rather than SNe Ic-BL/GRB-SNe. Despite a few similarities with SN 2006aj, PTF15dtg is not associated with a GRB/X-ray flash, and this could be because iPTF15dtg does not have or has a weaker central engine. This weak central engine might not be able to power a jet that breaks through the SN ejecta as in the case of GRB-SNe (Bromberg et al. 2011). However, a weaker central engine might be enough to produce the high degree of ^{56}Ni mixing that we observed in iPTF15dtg.

Our early light curve models depend on the fit of the main peak that we performed with hydrodynamical models. One limitation is that we exploded an He-rich star to produce the bolometric light curve of iPTF15dtg, despite the fact that this SN is likely He-poor. This is due to the difficulty of completely stripping the He layer with the current evolutionary models of single stars. However, we note that the He fraction of the progenitor stars of SE SNe should not significantly affect the bolometric light curve from the hydrodynamical model, as shown by Dessart et al. (2016) with their He-rich and He-poor models from binaries. The parameter of the progenitor star that mainly affects the SN bolometric light curve is its final mass, which we tuned to be $\sim$12 $M_\odot$. Another caveat concerning the hydrodynamical model is that SNEC is a 1D code and therefore we cannot take into account geometries that are different from spherical symmetry. Maeda et al. (2008), Modjaz et al. (2008), Taubenberger et al. (2009), and Valenti et al. (2012) indicate that a signature of bipolar explosions, typical of SNe with central engines, is a double peak in the profile of the nebular oxygen lines (even though the absence of a double peak does not rule out asphericity). We inspected the [O I] $\lambda\lambda$6300, 6364 line in our last spectrum (which is not fully nebular) and the double peak is not visible. Another limitation of our hydrodynamical model is that it is not fitted to the very early emission (cooling phase), but its parameters are used as input for the analytic models used to reproduce the early decline. Furthermore, to fit the bolometric light curve, we do not explore the entire parameter space, but we restrict the range of the parameters that we investigate by using the Arnett model and the metallicity measurement.

The presence of material around the SN progenitor (deduced from the early emission), and the large ejecta mass (deduced from the slow rise to the main peak) both point to a progenitor star with large initial mass. This type of star (e.g., a WR star with $M_{\rm ZAMS} \gtrsim 35\ M_\odot$) would be stripped of its outer layers by strong winds but would still leave $\sim$10 $M_\odot$ of ejecta, as estimated for iPTF15dtg. Furthermore, a massive WR star might be able to produce an extended CSM envelope through episodic mass-loss events occurring prior to collapse. The only possible example of a WR eruption is the massive outburst from the likely WR progenitor star of SN 2006jc, just a few years before collapse (Pastorello et al. 2007, but see also Corsi et al. 2014, on PTF11qcj). We note that, in the case of SN 2006jc, the outburst might also be explained in a scenario where the SN WR progenitor was in binary system with an LBV that erupted prior the collapse of the primary star.

If the 0.05 $M_\odot$ of the $R = 1200\ R_\odot$ extended envelope of iPTF15dtg are formed via an eruption, assuming a wind velocity of $\sim$1000 km s^{-1} (typical of massive WR stars, see e.g., Rochowicz & Niedzielski 1995) the envelope might have formed in a eruptive phase $\sim$10 days before collapse and characterized by extremely high mass-loss rate ($\dot{M} = 1.9\ M_\odot$ yr^{-1}). We stress that the extension and the mass of the envelope are lower limits (see Fig. 13. If we assume an envelope radius two times that of the best fit with a mass of 0.055 $M_\odot$ (which is still a good fit, see the bottom panel of Fig. 13), then the derived mass-loss rate would be about 1.0 $M_\odot$ yr^{-1}. If a large mass-ejection occurred in the weeks before explosion, this could have produced a pre-explosion outburst observable in the light curve, as in the case of SN 2006jc. The eruption event of SN 2006jc was observed at $\sim$4 mag below the main peak (Pastorello et al. 2007), peaking at ~ -14 mag. In the case of iPTF15dtg, our pre-explosion limits in g-band are not deep enough to detect such a faint outburst and they only cover limited time intervals between -75 d and 0 d. Furthermore, the extended envelope mass of iPTF15dtg is markedly lower than the shell ejected by the precursor of SN 2006jc (which was a strongly interacting SN Ibn) and hence the outburst of the progenitor for iPTF15dtg would have been even fainter.

The envelope properties of iPTF15dtg are more similar to those estimated for the mass surrounding SN IIb 2013cu (iPTF13ast; Gal-Yam et al. 2014), with a CSM extending at least $\sim$720 $R_\odot$ containing $\sim$0.004–0.017 $M_\odot$, produced by a mass-loss rate of $>$0.03 $M_\odot$ yr^{-1}. Similarly, Nakar (2015) finds the progenitor of SN 2006aj to be surrounded by an envelope larger than 100 $R_\odot$ and containing 0.01 $M_\odot$. In SN 2013cu, the presence of the envelope was marked by strong flash-spectroscopy emission lines which disappeared sometime after 3.23 d but before 6.45 d (Gal-Yam et al. 2014). Our first spectra for iPTF15dtg

[4] http://heasarc.gsfc.nasa.gov/w3browse/all/ipngrb.html

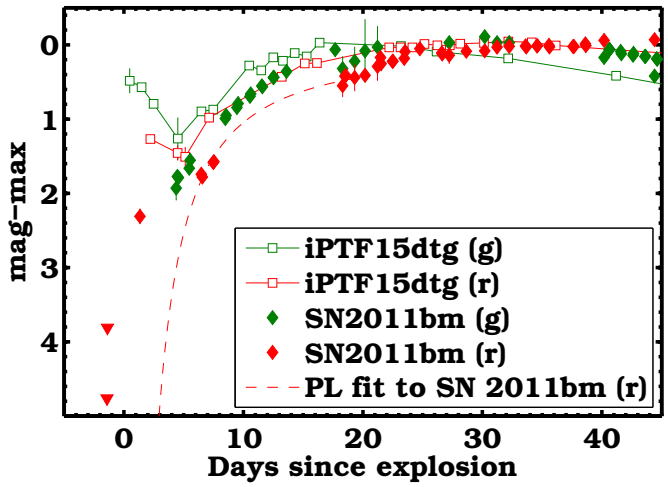

Fig. 14. Early time light curves (g and r-band) of iPTF15dtg (empty symbols) and SN 2011bm(=PTF11bov, filled symbols), with data from PTF and Valenti et al. (2012). Light curves are scaled to maximum. The early r-band data points reveal that there could be an excess in the emission of SN 2011bm, similar to what is observed for iPTF15dtg. The best power-law fit to the early data of SN 2011bm (excluding the first epoch) is shown by a dashed line.

were obtained at 3.2 ± 0.5 d and 4.5 ± 0.5 d, and they do not show these features.

There could be another explanation for the extended envelope. If the progenitor of iPTF15dtg was part of a binary system, and the progenitor explodes during a common envelope phase (Yoon 2015), this would imply a larger progenitor radius, consistent with the presence of a large envelope. The lack of flash spectroscopy signatures could also signal a different density profile of the SN environment, potentially due to binary evolution.

If extended envelopes are characteristic of massive WR progenitors of SNe Ic, we should find signatures of an early declining phase in the light curves of other long-rising SNe Ibc, which presumably have similar progenitors. For instance, we saw that iPTF15dtg is quite similar to SN 2011bm, both photometrically and spectroscopically. The light curves of SN 2011bm presented by Valenti et al. (2012) cover only one early epoch in the r-band, and thus it was difficult to asses the presence of an early declining phase. However, SN 2011bm was also observed by PTF (SN 2011bm=PTF11bov), with good coverage at early epochs in both g and r-band. In Fig. 14, we combine the data from Valenti et al. (2012) and PTF in r-band (and also in g-band), and it appears that the first r-band point of SN 2011bm displays an excess compared to the expected power-law (PL) rise (red dashed lines) obtained by fitting the early PTF r-band data points. Also in the case of SN 2011bm we thus have an early emission similar to that of iPTF15dtg, although with higher contrast with respect to the main peak. For the g-band, it is not possible to assess the presence of an early declining phase with a timescale similar to that of iPTF15dtg since the first observations occurred too late. For other (faster rising) SNe Ic this early excess is not present, as in the cases of SN 1994I (Sauer et al. 2006), PTF10vgv (Corsi et al. 2012; Piro 2015) or the SNe Ic presented by Taddia et al. (2015a). The early excess could be a common property of spectroscopically normal SNe Ic with slow rise, i.e., SN 2011bm-like events.

Slow rising SNe Ic (from massive WR stars) might be considered as bridging-gap objects between normal SNe Ib/c and SLSNe I, since their initial and ejecta masses are likely in-between those of the other two classes (Nicholl et al. 2015b). Normal SNe Ib/c may need the help of a companion to get rid of their H/He rich envelopes, whereas slow-rising SNe Ic and SLSN I might experience large enough mass-loss due to their stronger winds. Slow-rising SNe Ic such as iPTF15dtg and SN 2011bm show early peaks as do SLSNe I (Nicholl et al. 2015a), but the former are characterized by shorter timescales. As the timescale of the peaks are mainly dependent on the envelope mass, this implies larger envelope masses for SLSNe, compared to those of slow rising SNe Ic.

8. Conclusions

In this section, we list our conclusions as follows:

- iPTF15dtg is the first spectroscopically-normal SN Ic showing an early declining phase in the optical light curves.
- This SN also shows a long rise time, comparable only to that of SN 2011bm among SNe Ic.
- Analytic and hydrodynamical models of the main peak, as well as the fit to the expansion velocities, reveal a large ejecta mass of $\sim 10\ M_{\odot}$, with an explosion energy of $\sim 2 \times 10^{51}$ erg.
- The modeling of the early light curve decline favors the presence of an extended envelope surrounding the progenitor star. Shock breakout from the SN progenitor is excluded, whereas companion interaction or magnetar models are not favored.
- The large ejecta mass and the presence of extended material around the star suggest the progenitor star of iPTF15dtg was a massive Wolf-Rayet star, whose strong winds drove the stripping of the outer layers. It cannot be excluded that the WR star was in a binary system and exploded during a common envelope phase leading to the formation of the extended envelope.
- SN 2011bm is found to show an early excess similar to that of iPTF15dtg. This might be a common characteristic of slow rising SNe Ic.

Acknowledgements. We gratefully acknowledge the support from the Knut and Alice Wallenberg Foundation. This work is partly based on observations made with the Nordic Optical Telescope, operated by the Nordic Optical Telescope Scientific Association at the Observatorio del Roque de los Muchachos, La Palma, Spain, of the Instituto de Astrofisica de Canarias. The data presented here were obtained [in part] with ALFOSC, which is provided by the Instituto de Astrofisica de Andalucia (IAA) under a joint agreement with the University of Copenhagen and NOTSA. This work is partly based on observations made with DOLoRes@TNG. This paper made use of Lowell Observatory's Discovery Channel Telescope (DCT). Lowell operates the DCT in partnership with Boston University, Northern Arizona University, the University of Maryland, and the University of Toledo. Partial support of the DCT was provided by Discovery Communications. The Large Monolithic Imager (LMI) on DCT was built by Lowell Observatory using funds from the National Science Foundation (AST-1005313). LANL participation in iPTF was funded by the US Department of Energy as part of the Laboratory Directed Research and Development program. Part of this research was carried out at the Jet Propulsion Laboratory, California Institute of Technology, under a contract with the National Aeronautics and Space Administration. We thank N. Blagorodnova, E. Bellm, Y. Cao, G. Duggan, S. Kulkarni, J. Jencson, P. Nugent, for their precious help with the observations of iPTF15dtg and contribution to iPTF. We thank L. Yan for her comments on the paper. Based on observations obtained with the Samuel Oschin Telescope 48-inch and the 60-inch Telescope at the Palomar Observatory as part of the intermediate Palomar Transient Factory (iPTF) project, a scientific collaboration among the California Institute of Technology, Los Alamos National Laboratory, the University of Wisconsin, Milwaukee, the Oskar Klein Center, the Weizmann Institute of Science, the TANGO Program of the University System of Taiwan, and the Kavli Institute for the Physics and Mathematics of the Universe. A. Corsi acknowledges support from NSF CAREER Award #1455090.

References

Ahn, C. P., Alexandroff, R., Allende Prieto, C., et al. 2014, ApJS, 211, 17
Arcavi, I., Gal-Yam, A., Yaron, O., et al. 2011, ApJ, 742, L18
Arcavi, I., Gal-Yam, A., Kasliwal, M. M., et al. 2010, ApJ, 721, 777
Ben-Ami, S., Gal-Yam, A., Mazzali, P. A., et al. 2014, ApJ, 785, 37
Bersten, M. C., Tanaka, M., Tominaga, N., Benvenuto, O. G., & Nomoto, K. 2013, ApJ, 767, 143
Bianco, F. B., Modjaz, M., Hicken, M., et al. 2014, ApJS, 213, 19
Bromberg, O., Nakar, E., & Piran, T. 2011, ApJ, 739, L55
Brown, P. J., Holland, S. T., Immler, S., et al. 2009, AJ, 137, 4517
Campana, S., Mangano, V., Blustin, A. J., et al. 2006, Nature, 442, 1008
Cano, Z. 2013, MNRAS, 434, 1098
Cano, Z., Bersier, D., Guidorzi, C., et al. 2011, ApJ, 740, 41
Cano, Z., de Ugarte Postigo, A., Pozanenko, A., et al. 2014, A&A, 568, A19
Cano, Z., Wang, S.-Q., Dai, Z.-G., & Wu, X.-F. 2016, J. Adv. Astron., submitted [arXiv:1604.03549]
Cenko, S. B., Fox, D. B., Moon, D.-S., et al. 2006, PASP, 118, 1396
Chevalier, R. A. 1982, ApJ, 258, 790
Clocchiatti, A., Suntzeff, N. B., Covarrubias, R., & Candia, P. 2011, AJ, 141, 163
Corsi, A., Ofek, E. O., Gal-Yam, A., et al. 2012, ApJ, 747, L5
Corsi, A., Ofek, E. O., Gal-Yam, A., et al. 2014, ApJ, 782, 42
Djupvik, A. A., & Andersen, J. 2010, Astrophys. Space Sci. Proc., 14, 211
D'Elia, V., Pian, E., Melandri, A., et al. 2015, A&A, 577, A116
Dessart, L., Hillier, D. J., Woosley, S., et al. 2016, MNRAS, 458, 1618
Drout, M. R., Soderberg, A. M., Gal-Yam, A., et al. 2011, ApJ, 741, 97
Drout, M. R., Milisavljevic, D., Parrent, J., et al. 2016, ApJ, 821, 57
Eldridge, J. J., Fraser, M., Smartt, S. J., Maund, J. R., & Crockett, R. M. 2013, MNRAS, 436, 774
Ergon, M., Sollerman, J., Fraser, M., et al. 2014, A&A, 562, A17
Folatelli, G., Contreras, C., Phillips, M. M., et al. 2006, ApJ, 641, 1039
Filippenko, A. V. 1997, ARA&A, 35, 309
Filippenko, A. V., Barth, A. J., Matheson, T., et al. 1995, ApJ, 450, L11
Fremling, C., Sollerman, J., Taddia, F., et al. 2016, A&A, DOI: 10.1051/0004-6361/201628275
Fukugita, M., Ichikawa, T., Gunn, J. E., et al. 1996, AJ, 111, 1748
Gal-Yam, A. 2012, Science, 337, 927
Gal-Yam, A., Arcavi, I., Ofek, E. O., et al. 2014, Nature, 509, 471
Hunter, D. J., Valenti, S., Kotak, R., et al. 2009, A&A, 508, 371
Inserra, C., Smartt, S. J., Jerkstrand, A., et al. 2013, ApJ, 770, 128
Irwin, C. M., & Chevalier, R. A. 2016, MNRAS, 460, 1680
Kasen, D. 2010, ApJ, 708, 1025
Kasen, D., & Bildsten, L. 2010, ApJ, 717, 245
Kasen, D., Metzger, B. D., & Bildsten, L. 2016, ApJ, 821, 36
Komatsu, E., Dunkley, J., Nolta, M. R., et al. 2009, ApJS, 180, 330
Krühler, T., Malesani, D., Fynbo, J. P. U., et al. 2015, A&A, 581, A125
Kulkarni, S. R., Frail, D. A., Wieringa, M. H., et al. 1998, Nature, 395, 663
Leloudas, G., Chatzopoulos, E., Dilday, B., et al. 2012, A&A, 541, A129
Lunnan, R., Chornock, R., Berger, E., et al. 2014, ApJ, 787, 138
Lyman, J. D., Bersier, D., & James, P. A. 2014, MNRAS, 437, 3848
Lyman, J. D., Bersier, D., James, P. A., et al. 2016, MNRAS, 457, 328
Maeda, K., Tanaka, M., Nomoto, K., et al. 2007, ApJ, 666, 1069
Maeda, K., Kawabata, K., Mazzali, P. A., et al. 2008, Science, 319, 1220
Malesani, D., Fynbo, J. P. U., Hjorth, J., et al. 2009, ApJ, 692, L84
Margutti, R., Guidorzi, C., Lazzati, D., et al. 2015, ApJ, 805, 159
Mazzali, P. A., Deng, J., Nomoto, K., et al. 2006, Nature, 442, 1018
Mazzali, P. A., Valenti, S., Della Valle, M., et al. 2008, Science, 321, 1185
Modjaz, M., Kirshner, R. P., Blondin, S., Challis, P., & Matheson, T. 2008, ApJ, 687, L9
Modjaz, M., Li, W., Butler, N., et al. 2009, ApJ, 702, 226
Modjaz, M., Blondin, S., Kirshner, R. P., et al. 2014, AJ, 147, 99
Modjaz, M., Liu, Y. Q., Bianco, F. B., & Graur, O. 2016, ApJ, submitted [arXiv:1509.07124]
Morozova, V., Piro, A. L., Renzo, M., et al. 2015, ApJ, 814, 63
Nakar, E. 2015, ApJ, 807, 172
Nakar, E., & Piro, A. L. 2014, ApJ, 788, 193
Nicholl, M., & Smartt, S. J. 2016, MNRAS, 457, L79
Nicholl, M., Smartt, S. J., Jerkstrand, A., et al. 2015a, ApJ, 807, L18
Nicholl, M., Smartt, S. J., Jerkstrand, A., et al. 2015b, MNRAS, 452, 3869
Oke, J. B., Cohen, J. G., Carr, M., et al. 1995, PASP, 107, 375
Pastorello, A., Smartt, S. J., Mattila, S., et al. 2007, Nature, 447, 829
Paxton, B., Bildsten, L., Dotter, A., et al. 2011, ApJS, 192, 3
Perley, R. A., Chandler, C. J., Butler, B. J., & Wrobel, J. M. 2011, ApJ, 739, L1
Pettini, M., & Pagel, B. E. J. 2004, MNRAS, 348, L59
Piro, A. L. 2015, ApJ, 808, L51
Piro, A. L., & Nakar, E. 2013, ApJ, 769, 67
Prentice, S. J., Mazzali, P. A., Pian, E., et al. 2016, MNRAS, 458, 2973
Quimby, R. M., Kulkarni, S. R., Kasliwal, M. M., et al. 2011, Nature, 474, 487
Rahmer, G., Smith, R., Velur, V., et al. 2008, Proc. SPIE, 7014, 12
Rabinak, I., & Waxman, E. 2011, ApJ, 728, 63
Richmond, M. W., Treffers, R. R., Filippenko, A. V., et al. 1994, AJ, 107, 1022
Richmond, M. W., van Dyk, S. D., Ho, W., et al. 1996, AJ, 111, 327
Rochowicz, K., & Niedzielski, A. 1995, Acta Astron., 45, 307
Sanders, N. E., Soderberg, A. M., Levesque, E. M., et al. 2012, ApJ, 758, 132
Sanders, N. E., Levesque, E. M., & Soderberg, A. M. 2013, ApJ, 775, 125
Sauer, D. N., Mazzali, P. A., Deng, J., et al. 2006, MNRAS, 369, 1939
Schlafly, E. F., & Finkbeiner, D. P. 2011, ApJ, 737, 103
Smartt, S. J. 2009, ARA&A, 47, 63
Soderberg, A. M., Berger, E., Page, K. L., et al. 2008, Nature, 453, 469
Sollerman, J., Jaunsen, A. O., Fynbo, J. P. U., et al. 2006, A&A, 454, 503
Stritzinger, M., Hamuy, M., Suntzeff, N. B., et al. 2002, AJ, 124, 2100
Taddia, F., Sollerman, J., Razza, A., et al. 2013, A&A, 558, A143
Taddia, F., Sollerman, J., Leloudas, G., et al. 2015a, A&A, 574, A60
Taddia, F., Sollerman, J., Fremling, C., et al. 2015b, A&A, 580, A131
Taubenberger, S., Valenti, S., Benetti, S., et al. 2009, MNRAS, 397, 677
Taubenberger, S., Pastorello, A., Mazzali, P. A., et al. 2006, MNRAS, 371, 1459
Valenti, S., Elias-Rosa, N., Taubenberger, S., et al. 2008a, ApJ, 673, L155
Valenti, S., Benetti, S., Cappellaro, E., et al. 2008b, MNRAS, 383, 1485
Valenti, S., Fraser, M., Benetti, S., et al. 2011, MNRAS, 416, 3138
Valenti, S., Taubenberger, S., Pastorello, A., et al. 2012, ApJ, 749, L28
Waxman, E., Mészáros, P., & Campana, S. 2007, ApJ, 667, 351
Wheeler, J. C., Johnson, V., & Clocchiatti, A. 2015, MNRAS, 450, 1295
Woosley, S. E., & Bloom, J. S. 2006, ARA&A, 44, 507
Yaron, O., & Gal-Yam, A. 2012, PASP, 124, 668
Yoon, S.-C. 2015, PASA, 32, e015

Appendix A: Additional tables

Table A.1. Optical photometry of iPTF15dtg.

JD-2 457 000 (days)	B (mag)	JD-2 457 000 (days)	g (mag)	JD-2 457 000 (days)	r (mag)	JD-2 457 000 (days)	i (mag)
337.945	20.421(0.087)	333.931	19.634(0.162)	335.660	19.968(0.026)	335.662	20.308(0.037)
340.573	20.507(0.077)	334.931	19.720(0.029)	337.950	20.156(0.097)	337.953	20.671(0.122)
346.653	19.799(0.057)	335.931	19.943(0.027)	338.586	20.208(0.129)	340.589	20.499(0.100)
349.570	19.724(0.055)	337.948	20.383(0.082)	340.586	19.680(0.061)	346.664	19.465(0.036)
355.655	19.672(0.069)	337.960	20.412(0.278)	346.661	19.130(0.002)	348.582	19.324(0.010)
356.591	19.616(0.061)	338.584	20.288(0.109)	348.580	18.950(0.005)	349.602	19.257(0.028)
357.589	19.736(0.049)	339.933	20.046(0.012)	349.599	18.944(0.038)	355.655	19.084(0.008)
358.589	19.633(0.094)	340.584	20.028(0.071)	355.652	18.734(0.019)	356.598	19.027(0.027)
359.669	19.746(0.030)	340.936	20.022(0.015)	356.595	18.735(0.029)	357.599	19.018(0.024)
360.712	19.757(0.001)	343.941	19.427(0.012)	357.597	18.735(0.011)	358.596	18.977(0.033)
		344.941	19.494(0.049)	358.594	18.688(0.046)	359.687	18.946(0.020)
		345.951	19.318(0.021)	359.684	18.706(0.007)	360.721	18.917(0.016)
		346.659	19.392(0.027)	360.718	18.706(0.020)	361.592	18.911(0.052)
		346.759	19.363(0.005)	361.590	18.685(0.036)	363.582	18.908(0.027)
		347.738	19.259(0.004)	363.580	18.675(0.031)	365.616	18.857(0.026)
		348.578	19.293(0.013)	365.613	18.654(0.019)	367.584	18.846(0.053)
		348.750	19.306(0.050)	367.582	18.666(0.051)	369.581	18.896(0.030)
		349.597	19.268(0.045)	369.578	18.707(0.034)	380.421	19.051(0.035)
		349.827	19.120(0.053)	380.419	18.831(0.038)	386.443	19.031(0.025)
		355.650	19.207(0.015)	386.442	18.916(0.014)	393.355	19.087(0.026)
		356.593	19.187(0.036)	393.351	19.041(0.024)	398.357	19.274(0.041)
		356.634	19.165(0.001)	398.353	19.142(0.042)	400.424	19.244(0.043)
		357.595	19.242(0.001)	400.421	19.186(0.014)	410.417	19.213(0.059)
		358.591	19.245(0.055)	410.413	19.415(0.054)	413.372	19.440(0.023)
		359.615	19.240(0.010)	413.366	19.344(0.019)	413.623	19.429(0.001)
		359.682	19.284(0.007)	413.618	19.292(0.001)	416.639	19.472(0.001)
		360.716	19.307(0.008)	416.634	19.329(0.001)	420.678	19.442(0.001)
		361.588	19.257(0.046)	420.663	19.328(0.004)	423.679	19.562(0.007)
		363.578	19.331(0.037)	423.674	19.377(0.001)	441.619	19.784(0.003)
		365.604	19.395(0.030)	441.614	19.630(0.002)	444.701	19.801(0.001)
		365.612	19.332(0.010)	444.696	19.724(0.001)	448.639	19.877(0.001)
		367.579	19.391(0.069)	448.625	19.697(0.002)	451.638	19.960(0.084)
		369.576	19.475(0.050)	451.635	19.650(0.070)	458.355	19.905(0.022)
		374.636	19.565(0.021)	458.349	19.713(0.024)	463.378	19.838(0.031)
		380.417	19.942(0.088)	463.372	19.697(0.026)		
		386.439	19.944(0.022)				
		389.634	19.998(0.030)				
		393.347	20.099(0.024)				
		398.348	20.177(0.045)				
		400.416	20.292(0.022)				
		401.625	20.195(0.032)				
		410.407	20.414(0.093)				
		413.359	20.526(0.043)				
		413.615	20.411(0.002)				
		416.629	20.422(0.003)				
		423.669	20.465(0.006)				
		424.635	20.424(0.022)				
		427.655	20.434(0.243)				
		430.639	20.376(0.089)				
		444.691	20.645(0.001)				
		448.620	20.683(0.001)				
		451.642	20.620(0.068)				
		458.340	20.727(0.032)				
		463.356	20.768(0.032)				

Table A.2. Optical spectroscopy of iPTF15dtg.

Date (UT)	JD-2 457 000 (days)	Phase[a] (days)	Telescope	Instrument	Range (Å)
10 Nov. 2015	336.60	+3.2	TNG	DOLORES	3435−8076
11 Nov. 2015	337.98	+4.5	Keck1	LRIS	3074−10 278
23 Nov. 2015	350.46	+17.0	TNG	DOLORES	3561−10 462
02 Dec. 2015	358.85	+25.4	DCT	Deveny+LMI	3272−7731
06 Dec. 2015	362.50	+29.1	Keck1	LRIS	3070−10 232
10 Dec. 2015	367.43	+34.0	NOT	ALFOSC	3482−9083
10 Jan. 2016	398.32	+64.9	TNG	DOLORES	3382−9600
28 Jan. 2016	416.37	+82.9	NOT	ALFOSC	3463−9143
11 Feb. 2016	430.42	+97.0	TNG	DOLORES	3371−9609
09 Mar. 2016	456.73	+123.3	Gemini North	GMOS	3796−9346

Notes. [(a)] From explosion date.